

# Investigation of Amorphous/Nanocrystalline Iron-Based Thermal Barrier Coatings

K. Bobzin<sup>1</sup> · M. Öte<sup>1</sup> · T. Königstein<sup>1</sup>

Submitted: 30 May 2016/in revised form: 14 December 2016/Published online: 17 January 2017  
© ASM International 2017

**Abstract** Because of their favorable thermophysical properties, good machinability and low material costs, iron-based coatings which exhibit a highly amorphous/nanocrystalline microstructure are currently in the focus of research. Considering the crystallization temperature of the material, iron-based coatings might be the next generation of thermal barrier coatings (TBCs) for low-temperature systems, reducing thermal losses. The objective of this research project is the development of highly amorphous, iron-based coatings. For this purpose, amorphous feedstock materials with different chromium contents have been developed and characterized regarding their microstructures, phase compositions, crystallization temperatures and amorphous content. The results show that the amorphous content is reduced with increasing particle size and chromium content. The coatings were deposited by air plasma spraying (APS) and high-velocity oxygen fuel spraying (HVOF). It is shown that all coatings exhibit amorphous structures. HVOF coatings show a smaller amount of amorphous content compared to the feedstock materials, indicating crystallization occurring in not fully melted particles or insufficient rapid cooling. The APS process can increase the amount of amorphous content compared to the feedstock material, as shown for  $x_{Cr} = 15\%$ . All coatings proof good thermal shock

behavior. Lowest thermal diffusivity values were determined for APS coatings, which confirms the potential of iron-based TBCs.

**Keywords** amorphous metals · iron-based coatings · thermal barrier coatings

## Introduction

One of the most important purposes of thermal spray coatings is thermal insulation in order to protect the substrate material from excessive heat or to reduce heat losses of energy conversion systems. In case of high-temperature application, ceramic materials such as yttria-stabilized zirconia (YSZ) are established coating systems which have been investigated extensively. Further improvement regarding the thermal insulation properties of YSZ-based thermal barrier coatings (TBCs) can be achieved by altering microstructural characteristics, e.g., adjusting number, size, orientation and distribution of pores (Ref 1-3). In addition, research showed a relation between the thermal conductivity and the grain size of the material. By reducing the average grain size from  $d = 100$  nm to about  $d = 10$  nm, a reduction in thermal conductivity by a factor of two was observed. The reduction occurs due to higher density of grain boundaries hindering the heat flow (Ref 2). Following the equation expressing the relationship between thermal conductivity ( $\kappa$ ), specific heat capacity ( $c_p$ ), sound velocity within the material ( $v$ ) and mean free path ( $l$ ), the above-mentioned behavior can be explained.

$$\kappa = \frac{1}{3} \cdot c_p \cdot v \cdot l \quad (\text{Eq 1})$$

This article is an invited paper selected from presentations at the 2016 International Thermal Spray Conference, held on May 10-12, 2016, in Shanghai, P.R. China, and has been expanded from the original presentation.

✉ T. Königstein  
koenigstein@iot.rwth-aachen.de

<sup>1</sup> Surface Engineering Institute, RWTH Aachen University, Aachen, Germany

According to (Eq 1), a smaller mean free path reduces the thermal conductivity. The mean free path describes the traveling distance of phonons (lattice waves), which is the main transport mechanism of heat for non-metallic crystalline materials, between single scattering defects (Ref 4). These defects range from lattice defect to grain boundaries scattering high-frequency and low-frequency wavelengths, respectively (Ref 2). In conclusion, smaller grain sizes increase the density of scattering defects and thereby reduce the thermal conductivity.

In comparison with dielectric materials like ceramics, not only phonons but also electrons contribute to the thermal conductivity of metals. The overall conductivity of a metallic solid can be expressed as the sum of the contribution from the phonon and the electron transport. Therefore, metals are not known for their good thermal insulation properties. However, by increasing the amount of scattering defects, the thermal resistivity of metals can be increased. Scattering is caused by the interaction between phonons and electrons with any defects or imperfections in the metallic solids. The presence of differently sized atoms and impurities causes increased scattering (Ref 5). Materials such as metallic glasses, which consist of amorphous/nanocrystalline structures, exhibit higher amounts of scattering defects, resulting in better thermal insulation behavior in comparison with those with crystalline microstructure. Usually, the manufacturing of these so-called bulk metallic glasses (MG) is difficult and requires high cooling rates from liquid to solid state in order to suppress crystallization. The critical cooling rate can be influenced by the choice of alloy. Amiya et al. (Ref 6) investigated the bulk MG system FeBSiNb with regard to its glass-forming ability for different Nb concentrations by using mold casting and melt spinning. It was shown that by adding Nb, the critical thickness of this bulk MG alloy can be increased by a factor of 10. Bulk MGs have interesting properties such as high hardness and high yield strength. Ashby et al. (Ref 7) gave a detailed review about different attributes such as mechanical properties of MGs in comparison with crystalline metals, ceramics and polymers.

Thermal spraying is a modern, highly flexible coating technology, which allows the processing of different materials such as polymer, metals and ceramics. This technology uses different energy sources to heat and melt the feedstock material and to accelerate it toward the substrate. During impact, the particles solidify rapidly. For air plasma spraying (APS), the solidification times range in  $\mu\text{s}$  (Ref 8). During the APS process, feedstock materials are melted and accelerated by means of electrical energy changing the state of a gas mixture into a plasma state. Typical plasma gas mixtures consist of argon and hydrogen. Instead of plasma, high-velocity oxygen fuel spraying

(HVOF) operates with a continuous combustion of liquid or a gaseous fuel such as kerosene or propene and oxygen. The process temperatures are significantly lower for HVOF than for APS, which affects the choice of feedstock materials. Due to the higher particle velocity, the coatings deposited by HVOF exhibit a low porosity.

Previous scientists used thermal spraying to deposit nanocrystalline/amorphous metal coatings for different purposes. Zhang et al. (Ref 9) investigated the effect of different powder fractions on the tribological behavior of the coatings deposited by APS. All amorphous coatings showed better tribological performances with regard to wear resistance in comparison with the reference 316L. By using a finer powder fraction, the porosity was decreased compared to coarser powder fractions. Furthermore, the coating applied with the fine fraction exhibited the best wear resistance. Besides powder-based processes, wire-based processes can be used to deposit amorphous/nanocrystalline coatings. Arizmendi-Mirquecho et al. (Ref 10) used wire arc spraying technology and a cored wire to manufacture amorphous coatings on AISI 1018 carbon steel. Tribological testing confirmed a lower wear rate of the amorphous coating as opposed to the uncoated substrate. Besides wear, the excellent corrosion behavior of amorphous/nanocrystalline materials is in focus of research. Zhou et al. (Ref 11) investigated iron-based metallic glass coatings deposited by HVOF with regard to the corrosion behavior using different electrolytes such as NaCl, HCl and  $\text{H}_2\text{SO}_4$ . All coatings spontaneously passivated with a wide passive region and low current densities. These results show the potential of amorphous/nanocrystalline metal coatings applied by the thermal spray technology in the field of tribology and corrosion protection. Besides good tribological and corrosive behavior, amorphous/nanocrystalline coatings exhibit high densities of scattering defects which reduce the thermal conductivity to  $\kappa = 2 \text{ W/mK}$  (Ref 12, 13). The operation window of these materials is limited by their crystallization temperature, making them unattractive for high-temperature applications, such as turbines. Nevertheless, systems operating below crystallization temperature, such as combustion engines, can represent a suitable application area. Coatings applied on to the inner surface of engine cylinders can reduce heat losses and thereby increase the thermal efficiency. Typically, surface temperatures in this tribology system do not reach  $T = 200 \text{ }^\circ\text{C}$  and thereby operate below the crystallization temperatures. Furthermore, in comparison with YSZ, iron-based alloys have economic advantages due to their lower material costs and better mechanical properties such as higher ductility.

The present work summarizes the results with regard to the deposition of amorphous iron-based MG coatings

applied by HVOF and APS and investigates the effect of different coating technologies on the amount of amorphous structures within the coatings. Furthermore, the coatings were tested in an atmospheric thermocyclic furnace. In order to proof the thermal insulation properties of MGs, thermal diffusivities were measured by the laserflash method.

## Experimental Setup

Based on the results from previous research (Ref 6), a FeBSiNb alloy with the chemical composition  $x_{\text{Fe}} = 72$  at.%,  $x_{\text{Si}} = 4$  at.%,  $x_{\text{B}} = 20$  at.%,  $x_{\text{Nb}} = 4$  at.% was selected and further modified to improve corrosion resistance. Two modifications to the above-mentioned composition were designed by adding 5 and 15 at.% of chromium and reducing the iron content, respectively. The purpose of adding chromium was to improve the corrosion resistance considering a possible application area in combustion engines due to the utilization of exhaust gas recovery (EGR) systems. All three feedstock materials were manufactured by gas atomization and sieved subsequently with the aimed fraction of  $-20 + 45 \mu\text{m}$  for high-velocity oxygen fuel (HVOF) and  $-45 + 100 \mu\text{m}$  for air plasma spraying (APS).

In this study, two thermal spraying systems were used: F4 MB-XL torch by Oerlikon Metco (Winterthur, Switzerland), for APS and K2 torch by GTV-Verschleißschutz GmbH (Luckenbach, Germany) for HVOF. The following process parameters were used for the HVOF processes: kerosene fuel rate  $\dot{V}_{\text{K}} = 1.2 \text{ m}^3/\text{h}$ , powder carrier gas flow rate  $\dot{V}_{\text{N}_2} = 0.48 \text{ m}^3/\text{h}$ , oxygen flow rate  $\dot{V}_{\text{O}_2} = 48.0 \text{ m}^3/\text{h}$ , standoff distance  $s = 300 \text{ mm}$ , gun movement velocity  $v_{\text{g}} = 1.0 \text{ m/s}$ , nozzle length  $l_{\text{N}} = 145 \text{ mm}$  and nozzle diameter  $D_{\text{N}} = 12 \text{ mm}$ . The measured powder feedrate amounted to  $\dot{m}_{\text{p}} = 60 \text{ g/min}$ . For the APS process, the following parameter set was used: carrier gas flow rate  $\dot{V}_{\text{N}_2} = 0.24 \text{ m}^3/\text{h}$ , electric current  $I = 600 \text{ A}$ , standoff distance  $s = 120 \text{ mm}$ , argon flow rate  $\dot{V}_{\text{Ar}} = 2.22 \text{ m}^3/\text{h}$  and hydrogen flow rate  $\dot{V}_{\text{H}_2} = 0.6 \text{ m}^3/\text{h}$ , nozzle diameter  $D_{\text{N}} = 6 \text{ mm}$  and gun movement velocity  $v_{\text{g}} = 1.2 \text{ m/s}$ . The measured powder feedrate amounted to  $\dot{m}_{\text{p}} = 40 \text{ g/min}$ . All coatings were deposited on the aluminum substrate AlSi10, which is a common alloy for engine components. Prior to deposition, the substrates were grit-blasted using corundum F24 blasting medium with a grain size ( $x$ ) between  $x = 600$  and  $850 \mu\text{m}$  and cleaned with ethanol.

The particle size distribution of the feedstock materials was determined by optical means with the microscope Morphologi G2 by Malvern Instruments Ltd.

(Worcestershire, UK). This system captures pictures of the particles which were given onto a microscope slide. All particles are recognized by the software and quantified with regard to size. The particle microstructure and the coating microstructure were observed by scanning electron microscopy (SEM) using the microscope SEM LEO 1530 VP Gemini by Carl Zeiss AG (Oberkochen, Germany). The amorphous content of the feedstock materials and the coatings as well as the melting temperatures of the different feedstock materials were obtained by differential scanning calorimetry (DSC) using the system SETSYS Evolution from SETARAM Instrumentation (Caluire, France) with a heating rate of  $\dot{T} = 10 \text{ K/min}$ . All feedstock materials and coatings were investigated with regard to phase composition using x-ray diffraction (XRD) with the system Seifert XRD 3003 by GE Sensing & Inspection Technologies GmbH (Hürth, Germany). This machine uses a  $\text{CuK}\alpha$  target as radiation source. For measurements, the holding time was set to  $t_{\text{h}} = 10 \text{ s}$ , the step width was set to  $s = 0.05^\circ$ , and angle of incidence  $\omega$  was set to  $\omega = 10^\circ$ . The chemical composition of the feedstock materials was obtained by wet chemical analysis. In this analysis, the feedstock materials were dissolved in a mixture of HCl,  $\text{HNO}_3$  and HF. Subsequently, the solution was analyzed by means of inductively coupled plasma optical emission spectrometry (ICP-OES) with regard to the chemical composition. Using this method, even light elements such as boron can be quantified accurately. Thermal diffusivities of the coatings were measured by means of laserflash system FlashlineTM 4010 by Anter Corp. (Pittsburgh, USA). For the laserflash method, free-standing coatings were manufactured by depositing feedstock material on smooth steel substrates, which were mechanically detached subsequently. All specimens were segmented and grinded to a rectangular geometry with dimensions of  $10 \times 10 \times 1 \text{ mm}^3$ . During measurement, a laser heats up the surface of the samples. The temperature of the opposite surface is measured by an infrared detector. The higher the thermal diffusivity, the faster the temperature rises on the opposite side. Capturing the temperature-time relationship, thermal diffusivity can be obtained. Furthermore, proper samples were selected for cyclic heat exposition tests in an atmospheric furnace in order to evaluate the shock behavior. Therefore, segmented specimens were heat treated in an oven with a temperature of  $T_{\text{O}} = 400^\circ \text{ C}$  for  $t_{\text{e}} = 15 \text{ min}$ . The surface temperature ( $T_{\text{S}}$ ) measured by means of thermocouples amounted to about  $T_{\text{S}} = 300^\circ \text{ C}$ . After the heat treatment, the samples were cooled by the ambient atmosphere for  $t_{\text{A}} = 60 \text{ s}$ . Subsequently, compressed air was used to cool the samples with an increased cooling rate until the surface temperature reaches  $T_{\text{S}} = 50^\circ \text{ C}$ . The corresponding cooling rate is about  $\dot{T}_{\text{cool}} = 80^\circ \text{ C/min}$ . Considering a possible

application in combustion engines, the rapid cooling during the cyclic tests simulates harsh conditions, since the compact constructions of engines and heated cooling water inhibit a rapid cool down.

### Results and Discussion

The results of wet chemical analysis show good agreement with the aimed composition; see Table 1. No significant difference between different powder fractions can be recognized.

With regard to the size distribution of the different feedstock materials, no significant difference between  $x_{Cr} = 0, 5$  and  $15\%$  was observed; see Fig. 1. Both powder fractions fit to the aimed fraction,  $-20 + 45 \mu\text{m}$  for HVOF and  $-45 + 100 \mu\text{m}$  for APS.

SEM pictures of the particles show spherical shapes for all particles. Furthermore, satellites are recognized for all feedstock materials. Satellite formation seems to be more pronounced in case of the coarser feedstock material. In order to visualize the crystallinity, etched cross sections of single particles were prepared metallographically; see Fig. 2. It can be seen that for  $x_{Cr} = 15\%$ , both powder fractions exhibit a highly crystalline microstructure; see Fig. 2(e) and (f). For the  $x_{Cr} = 0$  and  $5\%$ , a difference with regard to particle size is recognizable. The finer powder fraction ( $-20 + 45 \mu\text{m}$ ) exhibits less crystallinity than the coarser powder fraction ( $-45 + 100 \mu\text{m}$ ). Therefore, it can be stated that the crystallinity increases with the particle size and chromium content in the examined range. The effect of particle size can be explained by the cooling rates during the atomization process of the feedstock materials. Smaller particles exhibit a larger surface-to-volume ratio, allowing them to cool more rapidly than larger particles, thus suppressing the crystallization.

Results of XRD measurements support the results derived by means of visual inspection of the cross section of powder particles; see Fig. 3. All the coarse feedstock materials examined in this study show an intense peak which is an indication of crystallinity; see Fig. 3(a). The

**Table 1** Chemical composition of HVOF and APS feedstock materials in at.%

Feedstock material	Process	Fe	Cr	B	Si	Nb
$x_{Cr} = 0$	HVOF	68.5	...	21.5	4.8	5.3
$x_{Cr} = 5$	HVOF	61.7	6.1	22.0	4.9	5.3
$x_{Cr} = 15$	HVOF	51.5	16.6	21.8	4.9	5.2
$x_{Cr} = 0$	APS	69.7	0	21.1	4.5	4.7
$x_{Cr} = 5$	APS	63.2	6.1	21.4	4.6	4.7
$x_{Cr} = 15$	APS	53.7	15.9	21.1	4.5	4.7

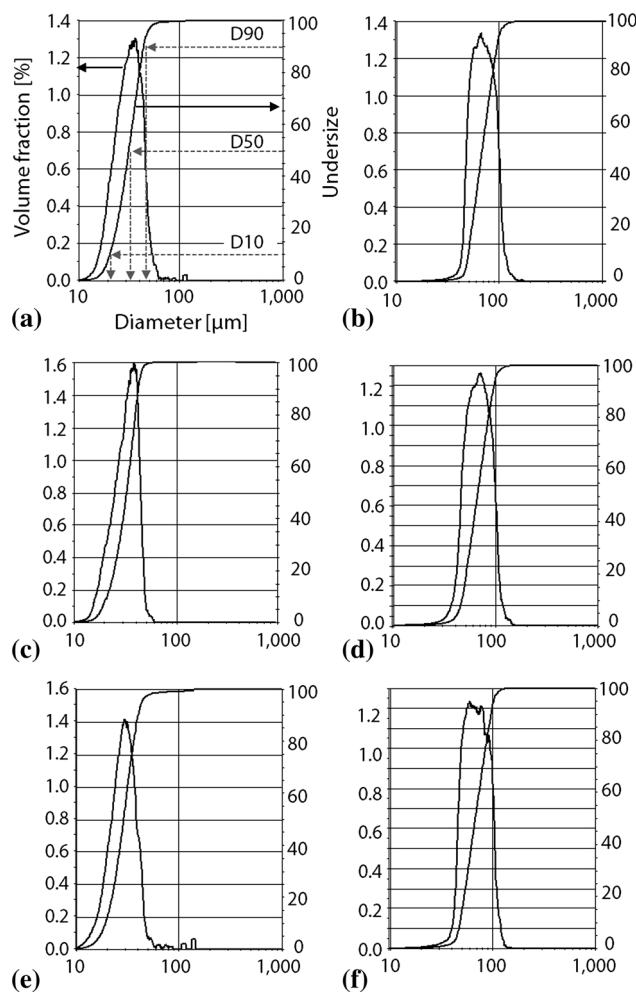


**Fig. 1** Particle size distribution referred to the volume: (a) HVOF  $x_{Cr} = 0\%$ , (b) APS  $x_{Cr} = 0\%$ , (c) HVOF  $x_{Cr} = 5\%$ , (d) APS  $x_{Cr} = 5\%$ , (e) HVOF  $x_{Cr} = 15\%$ , (f) APS  $x_{Cr} = 15\%$

fine feedstock materials, which were used for the HVOF process, show different results. In particular, no intense peak can be detected during the measurements of  $x_{Cr} = 0$  and  $5\%$ , indicating an amorphous structure.

In order to evaluate the influence of chromium on the melting temperatures ( $T_m$ ), DSC measurements were taken. In addition, glass transition temperatures ( $T_g$ ), crystallization temperatures ( $T_x$ ) and liquidus temperatures ( $T_l$ ) were detected and analyzed. Figure 4(a) and (b) shows the characteristic temperatures measured for the finer feedstock materials used for HVOF. For  $x_{Cr} = 0\%$ , the temperatures correspond to  $T_g = 540 \text{ }^\circ\text{C}$ ,  $T_x = 580 \text{ }^\circ\text{C}$ ,  $T_m = 1125 \text{ }^\circ\text{C}$  and  $T_l = 1155 \text{ }^\circ\text{C}$ . Increasing the chromium content to  $x_{Cr} = 15\%$  results in a temperature shift in all characteristic temperatures with a value of about  $\Delta T = 60 \text{ }^\circ\text{C}$  to higher values. This influences the microstructure of the deposited coatings due to the inclusion of partially melted particles. This will be discussed in the following.

**Fig. 2** Etched, polished cross sections of feedstock materials: (a)  $x_{Cr} = 0\%$  for HVOF process, (b)  $x_{Cr} = 0\%$  for APS process, (c)  $x_{Cr} = 5\%$  for HVOF process, (d)  $x_{Cr} = 5\%$  for APS process, (e)  $x_{Cr} = 15\%$  HVOF process, (f)  $x_{Cr} = 15\%$  APS process

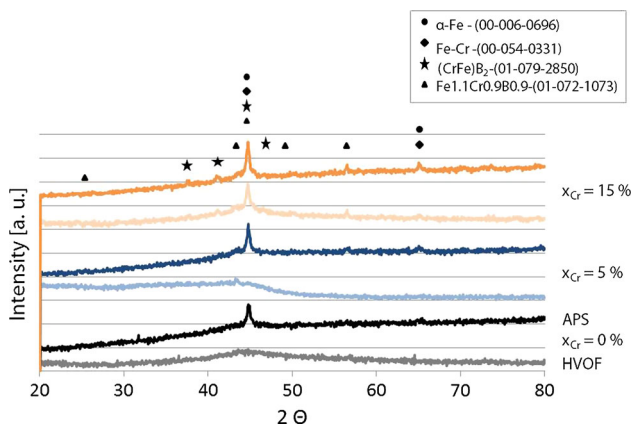
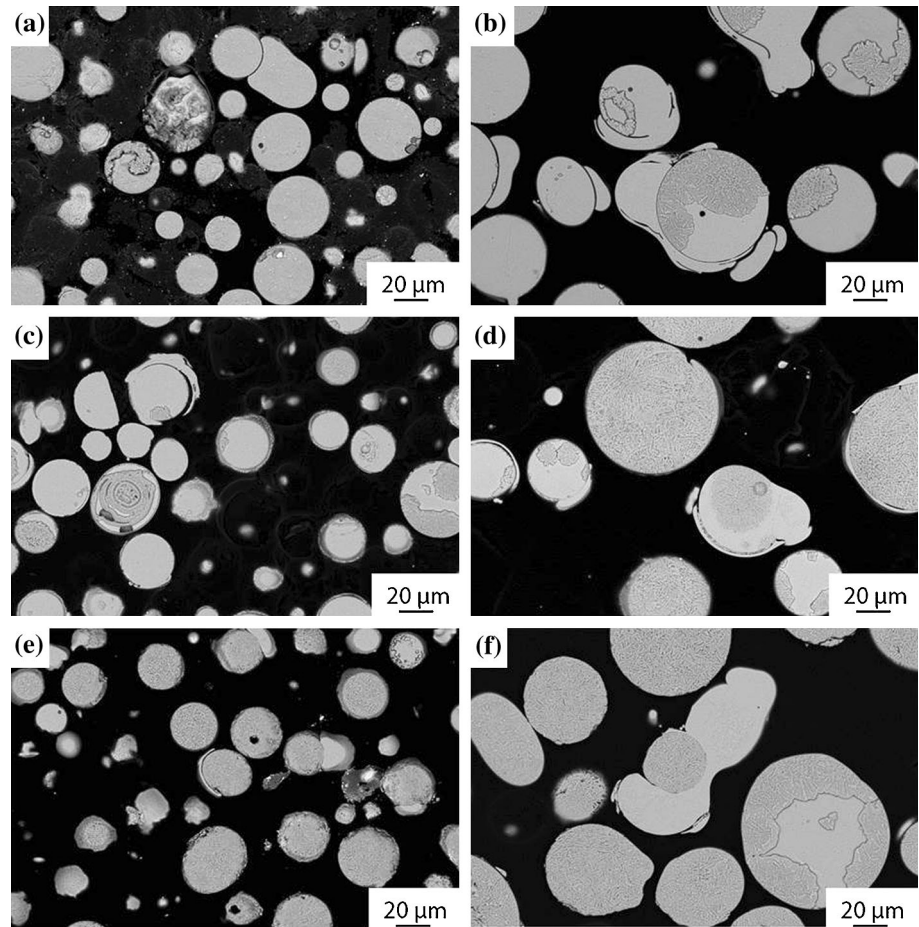


**Fig. 3** XRD measurements of different feedstock materials

Evaluating the crystallization enthalpy, the DSC measurements can prove the presence of amorphous structures and furthermore allow assumptions regarding the amount of amorphous structures within a material. Therefore, a reference specimen, which exhibits pure amorphous structures, is required. In this study, these reference specimens were manufactured by means of the melt spinning

process, employing high cooling rates to manufacture amorphous ribbons. In Fig. 5(a), the results of DSC measurements of the ribbons produced with three different compositions show distinctive exothermic peaks indicating the crystallization behavior of the material. However, different appearances can be identified. While for  $x_{Cr} = 0$  and 5% two crystallization peaks can be found, indicating the formation of different crystalline structures, the high chromium content material  $x_{Cr} = 15\%$  shows only one peak. The dashed lines represent the second heating cycle, proving that 100% of the material was crystallized during the first heating cycle. Considering the baseline integral value below the crystallization peak, the crystallization enthalpy ( $E_{C,R}$ ) which is released for the formation of crystalline structures can be determined. Compared to the ribbons, all three feedstock materials show similar characteristics. Figure 5(b) shows the runs of the DSC measurements for  $x_{Cr} = 0\%$  and both powder fractions exemplarily, showing that the fraction does not affect the characteristic temperatures.

By determining crystallization enthalpies of the feedstock materials ( $E_{C,P}$ ) and comparing these to the crystallization enthalpy of the ribbons, assumptions regarding the

**Fig. 4** DSC measurements for the fine powder fractions for HVOF process: (a) crystallization behavior, (b) melting behavior

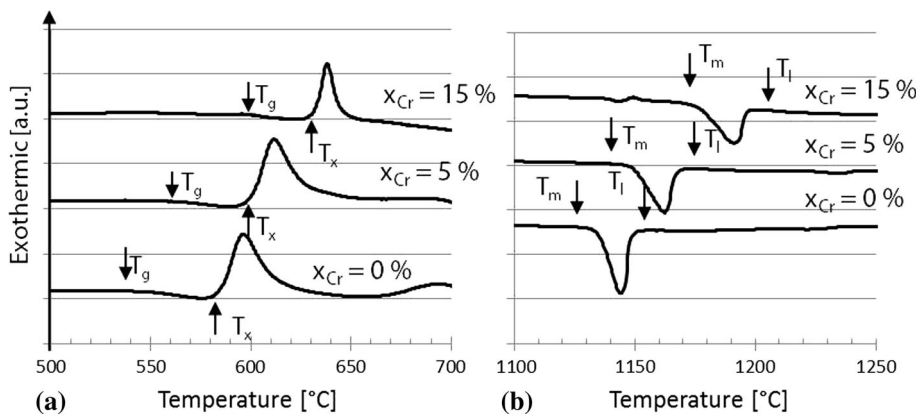


**Fig. 5** Crystallization energy release of (a) ribbons and (b) powder fine and coarse fraction for composition  $x_{Cr} = 0\%$

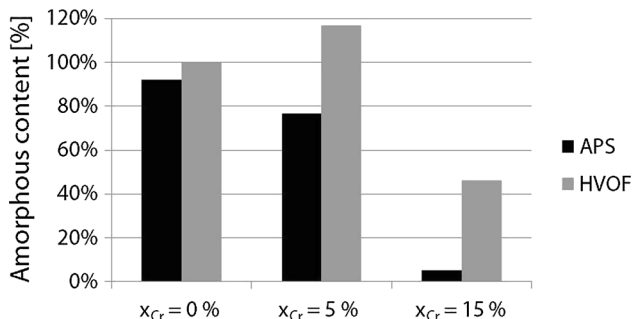
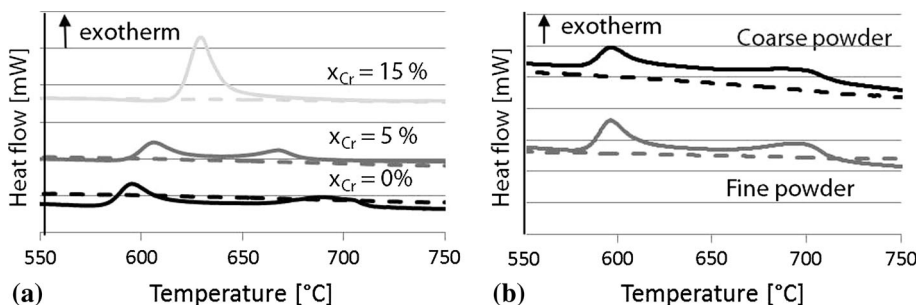


**Fig. 6** Calculated amorphous contents of the feedstock materials

amorphous content ( $x_{Am} = \frac{E_{C,P}}{E_{C,R}}$ ) can be made. This approach is consistent with the former studies dealing with crystallinity of metallic glasses (Ref 11, 14). Although the course of the DSC curves for fine and coarse powder fractions is similar, the crystallization enthalpy of all coarse powder fractions is smaller than fine powder fractions, showing that the crystalline structures are more dominant in coarse powder fractions; see Fig. 6. In case of  $x_{Cr} = 5$  and 15%, the difference in amorphous contents for coarse and fine powder fractions becomes more pronounced. Furthermore, Fig. 6 shows that the feedstock material with highest chromium content exhibits the highest crystallinity. These results are in line with the XRD measurements and metallographic analysis of the polished cross sections.

After the characterization of the feedstock materials, coating experiments were conducted. The coatings were analyzed with the same methodology as the feedstock materials. The polished cross section of the coating deposited with  $x_{Cr} = 15\%$  and using HVOF shows a high amount of unmolten particles within the coating; see Fig. 7(c). This can be attributed to the higher melting temperatures of the feedstock material, which is already proven by DSC; see Fig. 4(b). As a consequence, the particles are more likely to bounce after the impact and get lost in the overspray, reducing the deposition efficiency. Coatings deposited with  $x_{Cr} = 0$  and 5% reveal a typical lamellar microstructure. The porosities of all HVOF coatings amount to about  $p = 2-3\%$  and do not change across different feedstock materials.

In contrast to the HVOF coatings, the APS coatings exhibit a more pronounced, inhomogeneous microstructure; see Fig. 8. This can be attributed to the plasma fluctuations. The porosity is significantly higher, corresponding to  $p = 6-10\%$ . From the polished cross sections in Fig. 8, it can be seen that the coating deposited with the feedstock material  $x_{Cr} = 15\%$  exhibits highly deformed and flattened splats resulting in a lamellar coating microstructure in comparison with that with HVOF. It is assumed that the higher process temperatures are responsible for a better deformability of the particles during impact. Moreover, the polished cross sections show vertically running cracks which presumably appear due to intrinsic residual stresses.

**Fig. 7** Polished cross sections of HVOF coatings:

(a)  $x_{Cr} = 0\%$ , (b)  $x_{Cr} = 5\%$ ,  
(c)  $x_{Cr} = 15\%$

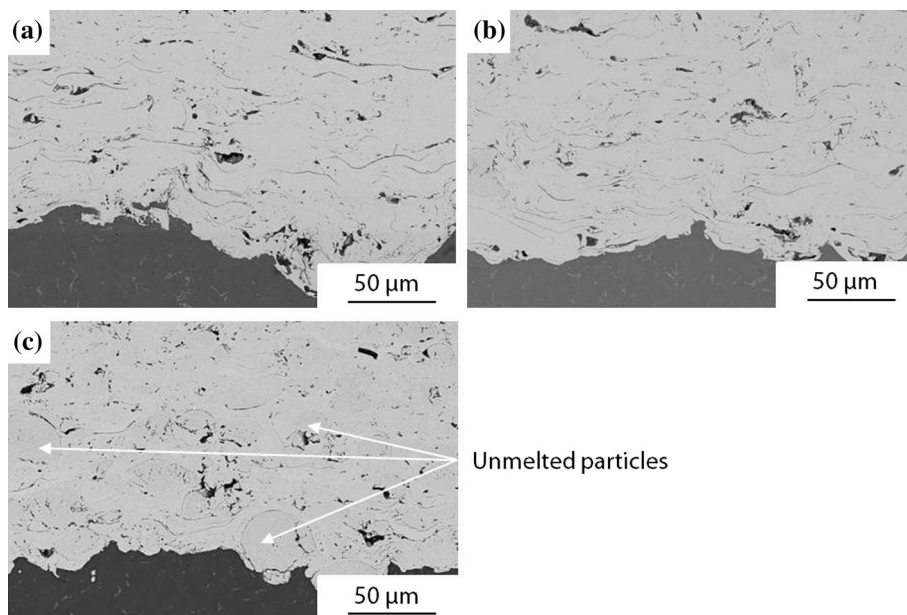
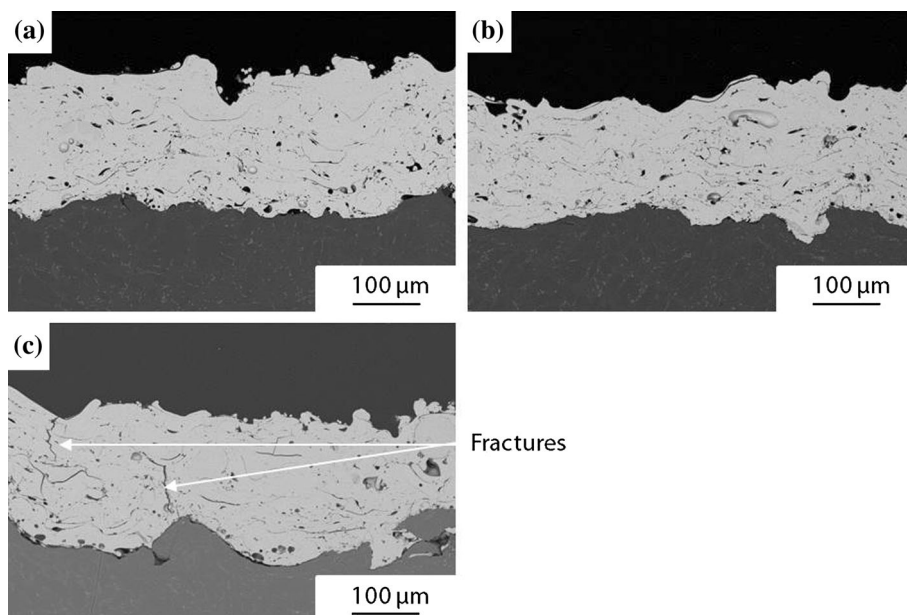


**Fig. 8** Polished cross sections of APS coatings: (a)  $x_{Cr} = 0\%$ ,  
(b)  $x_{Cr} = 5\%$ , (c)  $x_{Cr} = 15\%$



Due to the fact that these cracks were not identified for  $x_{Cr} = 0$  and 5%, it is assumed that the addition of high  $x_{Cr} = 15\%$  chromium negatively affects the thermophysical properties of the coating material.

The phase composition and calculated amount of amorphous structures can be found in Fig. 9. By comparing the XRD results, it can be seen that all HVOF coatings exhibit a broad intensity peaks at  $2\Theta = 45^\circ$ . The peak becomes sharper and more intense for  $x_{Cr} = 15\%$ , indicating an increased crystallinity. Measurements of APS coatings represent horizontally running trends. All XRD

measurements of APS coatings show a low intensity peak at  $2\Theta = 45^\circ$ . Furthermore, it can be observed that for APS coatings the intensity peak increases with decreasing chromium content, indicating the highest amount of crystalline structures for  $x_{Cr} = 0\%$ . DSC measurements and determination of the amorphous content as described above underline these assumptions. The lowest amount of amorphous structures for the HVOF coatings can be found for  $x_{Cr} = 15\%$ . Coatings deposited by APS exhibit amorphous contents following the reciprocal trend of the XRD signal intensity, also proving the above-mentioned assumptions.

**Fig. 9** XRD measurement and calculated amorphous content of HVOF and APS coatings

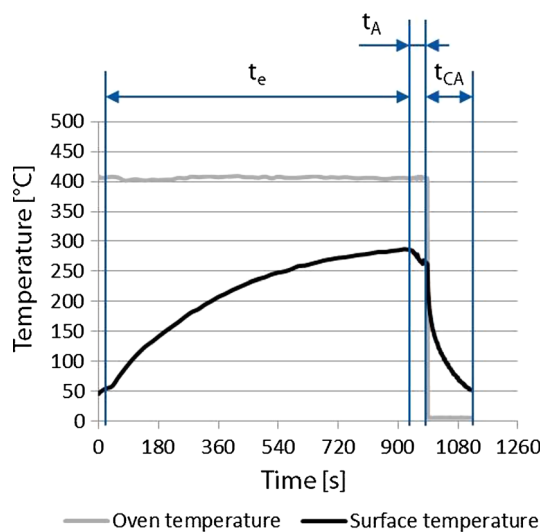
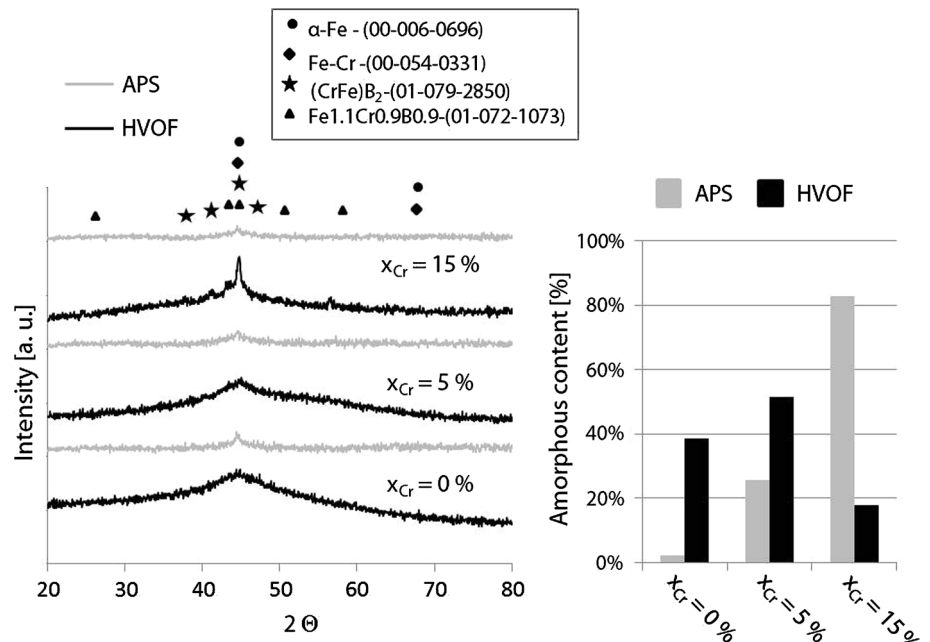


**Fig. 10** Surface temperature during thermocyclic test

The biggest discrepancy between APS and HVOF coatings can be found for  $x_{Cr} = 15\%$ , which will be explained in the following. For  $x_{Cr} = 15\%$  coatings deposited by HVOF, it is assumed that either the process temperatures are too small or that the exposition time of the particles in the flame is too short to melt the feedstock material. The cross-sections of the manufactured HVOF coating exhibit a high degree of unmolten particles, which obviously did not reach a liquid state during flight. Thereby, the highly crystalline structure of the particles is directly transferred into the coating, exhibiting an even higher amount of crystalline structures due to further crystallization of the particles

during flight, see Figs. 6 and 9. Using  $x_{Cr} = 15\%$  in combination with the APS fully melts the particles and transfers the particles into an amorphous, liquid state. Cross-sections prove that due to the lamellar structure. After the impact with the substrate, very short solidification times suppress the crystallization of the feedstock. As a result, a highly amorphous coating is formed.

After the evaluation of the cross sections, all coatings except for coating system  $x_{Cr} = 15\%$  deposited by APS were selected for a cyclic heat test in which they were compared to a reference. As a reference, a coating system consisting of MCrAlY bond coat and YSZ top coating was manufactured. Figure 10 represents the temperature curve of the sample during one of the 1000 heating cycles.

In order to investigate the shock behavior, polished cross sections were manufactured subsequently to the heat exposition test; see Fig. 11. Neither before nor after the thermocyclic test do any of the samples, including the reference, show any macrocracks. This is an indicator for good thermal shock behavior of the developed iron-based amorphous coatings. Please note that the difference between the thicknesses of HVOF and APS coatings is due to the different number of torch passes.

In order to investigate the insulation properties of the material, the thermal diffusivities were determined with the laserflash method. Therefore, free-standing coatings were manufactured. The results show that metallic glasses exhibit thermal diffusivity values which are 3-5 times lower compared to steel grade S235JR; see Fig. 12. As expected, the reference, plasma-sprayed YSZ, exhibits the lowest values. All thermal diffusivities of amorphous iron-based coatings range between  $\alpha = 0.01$  and  $0.04 \text{ cm}^2/\text{s}$ .



**Fig. 11** Polished cross sections after thermocyclic test (a) HVOF,  $x_{Cr} = 0\%$ ; (b) APS,  $x_{Cr} = 0\%$ ; (c) HVOF,  $x_{Cr} = 5\%$ ; (d) APS,  $x_{Cr} = 5\%$ ; (e) HVOF,  $x_{Cr} = 15\%$ ; (f) reference

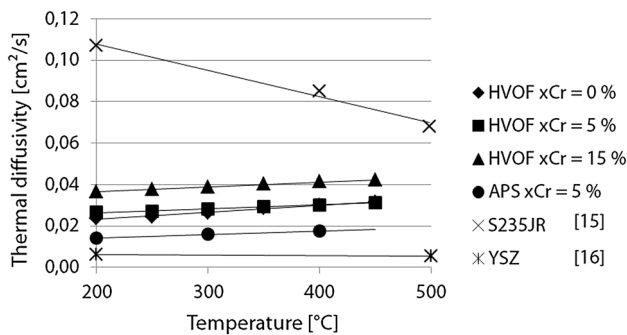
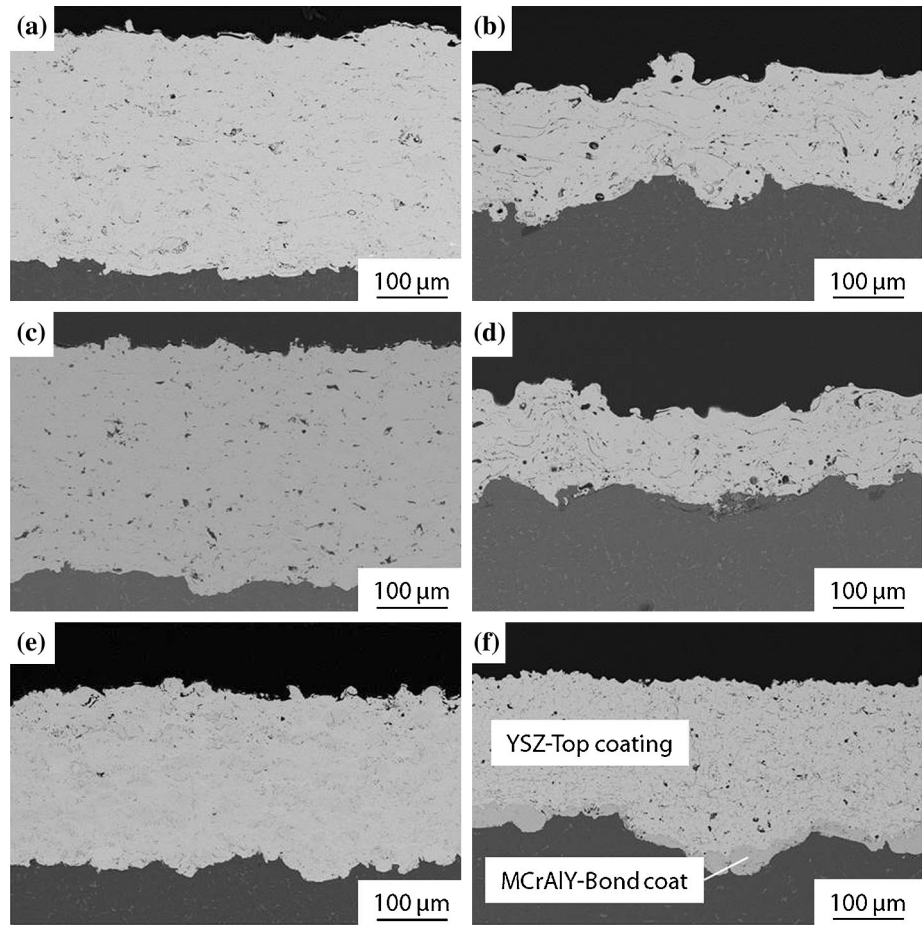


**Fig. 12** Thermal diffusivity of HVOF and APS coatings in comparison with steel grade S235JR and YSZ plasma-sprayed coatings

The HVOF coating with  $x_{Cr} = 15\%$  exhibits the highest thermal diffusivity. However, the porosity of this system is in a very similar range to those of HVOF coatings deposited with  $x_{Cr} = 0$  and  $5\%$ . Therefore, it can be assumed that the high amount of crystalline structures is responsible for the high thermal diffusivity of this coating system. The APS coating exhibits the lowest thermal diffusivity. In this case, the higher amount of porosity in combination with the amorphous structures might be responsible for the low value measured.

## Conclusion and Future Outlook

In this study, amorphous metallic feedstock materials with different chromium contents were investigated with regard to their amorphous contents. It has been shown that an increase in particle size and chromium content reduces the amorphous content. Metallic glass coatings were manufactured by HVOF and APS processes. The HVOF coatings exhibit a more homogenous microstructure and lower porosity than the APS coatings. Due to lower process temperatures of the HVOF process, a high amount of unmolten particles can be found in the coating deposited with  $x_{Cr} = 15\%$ . Using APS and  $x_{Cr} = 15\%$ , a lamella microstructure can be identified in the polished cross section. Selected samples were exposed to the cyclic heat test in an atmospheric furnace. Neither HVOF nor APS coatings show cracks after the thermal cycling exposition. Investigations with regard to the thermal diffusivities proved low values over a wide temperature range. Although all HVOF coatings examined in this study exhibit similar porosities, different thermal diffusivities were measured for these coating systems by means of the laserflash method. Specifically, the HVOF coating with

$x_{Cr} = 15\%$  showed the smallest amorphous phase content and the highest thermal diffusivity, indicating a relation between the thermal diffusivity and amount of amorphous structure.

For future work, the application of the developed feedstock materials onto the inner geometries, i.e., onto the inner surface of motor cylinder wall, will be investigated by plasma transferred wire arc (PTWA) technology. For this purpose, the developed feedstock material will be produced in form of wire. Furthermore, the influence of crystalline and amorphous structures on thermophysical properties, such as thermal diffusivity, will be investigated more deeply.

**Acknowledgments** The authors gratefully acknowledge the financial support of the German Research Foundation (DFG) within the Project ‘Basic research on the applicability of Fe-based TS-coating with the purpose of thermal insulation’ (BO 1979/34-1).

## References

1. H. Yang, J.A. Eastman, L.J. Thompson, and G.R. Bai, Grain-Size-Dependent Thermal Transport Properties in Nanocrystalline Ytria-Stabilized Zirconia, *Mater. Res. Soc.*, 2002, **703**, p 179-184
2. P.G. Klemens and M. Gell, Thermal Conductivity of Thermal Barrier Coatings, *Mater. Sci. Eng.*, 1993, **A245**, p 143-149
3. K. Bobzin, L. Zhao, M. Öte, and T.F. Linke, Deposition and Characterization of Thermal Barrier Coatings of  $ZrO_2$ —4 mol.%  $Y_2O_3$ —1 mol.%  $Gd_2O_3$ —1 mol.%  $Yb_2O_3$ , *Surf. Coat. Technol.*, 2015, **268**, p 205-208
4. K.T. Regner, D.R. Sellan, Z. Su, C.H. Amon, A.J.H. McGaughesy, and J.A. Malen, *Broadband Phonon Mean Free Path Contributions to Thermal Conductivity Measured Using Frequency Domain Thermoreflectance*, *Commun. Nat*, 2013, doi:[10.1038/ncomms2630](https://doi.org/10.1038/ncomms2630)
5. J.L. Plawsky, *Transport Phenomena Fundamentals*, 3rd ed., p 95
6. K. Amiya, A. Urata, N. Nishiyama, and A. Inoue, Fe–B–Si–Nb Bulk Metallic Glasses with High Strength above 4000 MPa and Distinct Plastic Elongation, *Mater. Trans.*, 2004, **45**(4), p 1214-1218
7. M.F. Ashby and A.L. Greer, *Metallic Glasses as Structural Materials*, *Scr. Mater.*, 2006, **54**, p 321-326
8. C. Moreau, P. Cielo, and M. Lamontagne, Flattening and Solidification of Thermally Sprayed Particles, *J. Therm. Spray Technol.*, 1992, **1**(4), p 317-323
9. H. Zhang, Y. Xie, L. Huang, S. Huang, X. Zheng, and G. Chen, Effect of Feedstock Particle Size on Wear Resistance of Plasma Sprayed Fe-Based, Amorphous Coatings, *Surf. Coat. Technol.*, 2014, **258**, p 495-502
10. A. Arizmendi-Morquecho, A. Campa-Castilla, C. Leyva-Porras, J.A.A. Martinez, G.V. Gutierrez, K.J.M. Bello, and L.L. Lopez, Microstructural Characterization and Wear Properties of Fe-Based Amorphous-Crystalline Coating Deposited by Twin Wire Arc Spraying, *Adv. Eng. Mater.*, 2014, doi:[10.1155/2014/836739](https://doi.org/10.1155/2014/836739)
11. Z. Zhou, L. Wang, F.C. Wang, H.F. Zhang, Y.B. Liu, and S.H. Xu, Formation and Corrosion Behavior of Fe-Based Amorphous Metallic Coatings by HVOF Thermal Spraying, *Surf. Coat. Technol.*, 2009, **204**, p 563-570
12. D. Shin, F. Gitzhofer, and C. Moreau, Properties of Induction Plasma Sprayed Iron Based Nanostructured Alloy Coatings for Metal Based Thermal Barrier Coatings, *J. Therm. Spray Technol.*, 2007, **16**(1), p 118-127
13. D. Shin, F. Gitzhofer, and C. Moreau, Thermal Property Evolution of Metal Based Thermal Barrier Coatings with Heat Treatments, *J. Mater. Sci.*, 2007, **42**, p 5915-5923
14. S. Kumar, J. Kim, H. Kim, and C. Lee, Phase Dependence of Fe-Based Bulk Metallic Glasses on Properties of Thermal Spray Coatings, *J. Alloy. Compd.*, 2009, **475**(1), p L9-L12
15. M. Iordachescu, J. Ruiz-Hervias, D. Iordachescu, A. Valiente, and L. Caballero, Thermal Influence of Welding Process on Strength Overmatching of Thin Dissimilar Sheets Joints, *Iberian Conference on Fracture and Structural Integrity*, 2010
16. L. Jin, P. Li, H. Zhou, W. Zhang, G. Zhou, and C. Wang, *Prog. Nat. Sci. Mater. Int.*, 2014, **25**, p 141-146